HAL
open science

Four-Spacecraft Measurements of the Shape and Dimensionality of Magnetic Structures in the Near-Earth Plasma Environment

S Fadanelli, B. Lavraud, F. Califano, C. Jacquey, I. Kacem, Y. Vernisse, E. Penou, D J Gershman, J Dorelli, C. Pollock, et al.

To cite this version:

S Fadanelli, B. Lavraud, F. Califano, C. Jacquey, I. Kacem, et al.. Four-Spacecraft Measurements of the Shape and Dimensionality of Magnetic Structures in the Near-Earth Plasma Environment. Journal of Geophysical Research Space Physics, 2019, 124 (8), pp.6850-6868. 10.1029/2019JA026747 . hal-02325587

HAL Id: hal-02325587

https://hal.science/hal-02325587v1

Submitted on 22 Oct 2019

HAL is a multi-disciplinary open access archive for the deposit and dissemination of scientific research documents, whether they are published or not. The documents may come from teaching and research institutions in France or abroad, or from public or private research centers.

L'archive ouverte pluridisciplinaire **HAL**, est destinée au dépôt et à la diffusion de documents scientifiques de niveau recherche, publiés ou non, émanant des établissements d'enseignement et de recherche français ou étrangers, des laboratoires publics ou privés.

JGR Space Physics

RESEARCH ARTICLE
10.1029/2019JA026747

Key Points:
- We define and use a four-spacecraft method on MMS data to study the magnetic field configuration at small scales in near Earth regions
- Case studies demonstrate the ability of the method to measure local magnetic configuration, benchmarking the method on previous studies
- Statistically, low plasma betas are correlated with large length scales and slightly more frequent planar shapes in magnetic configurations

Supporting Information:
- Supporting Information S1

Correspondence to:
S. Fadanelli,
sid.fadanelli@irap.omp.eu

Citation:
Fadanelli, S., Lavraud, B., Califano, F., Jacquey, C., Vernisse, Y., Kacem, I., et al. (2019). Four-spacecraft measurements of the shape and dimensionality of magnetic structures in the near-Earth plasma environment. *Journal of Geophysical Research: Space Physics*, *124*, 6850–6868. https://doi.org/10.1029/2019JA026747

Received 20 MAR 2019
Accepted 10 JUN 2019
Accepted article online 18 AUG 2019
Published online 30 AUG 2019

©2019. American Geophysical Union. All Rights Reserved.

Four-Spacecraft Measurements of the Shape and Dimensionality of Magnetic Structures in the Near-Earth Plasma Environment

S. Fadanelli[1,2], B. Lavraud[1], F. Califano[2], C. Jacquey[1], Y. Vernisse[1], I. Kacem[1], E. Penou[1], D. J. Gershman[3], J. Dorelli[3], C. Pollock[3], B. L. Giles[3], L. A. Avanov[3], J. Burch[4], M. O. Chandler[5], V. N. Coffey[5], J. P. Eastwood[6], R. Ergun[7], C. J. Farrugia[8], S. A. Fuselier[4,9], V. N. Genot[1], E. Grigorenko[10], H. Hasegawa[11], Y. Khotyaintsev[12], O. Le Contel[13], A. Marchaudon[1], T. E. Moore[3], R. Nakamura[14], W. R. Paterson[3], T. Phan[15], A. C. Rager[3], C. T. Russell[16], Y. Saito[11], J.-A. Sauvaud[1], C. Schiff[3], S. E. Smith[3], S. Toledo Redondo[1], R. B. Torbert[8], S. Wang[17], and S. Yokota[18]

[1]Institut de Recherche en Astrophysique et Planétologie, CNRS, UPS, CNES, Université de Toulouse, Toulouse, France, [2]Dipartimento di Fisica, Università di Pisa, Pisa, Italy, [3]NASA Goddard Space Flight Center, Greenbelt, MD, USA, [4]Southwest Research Institute, San Antonio, TX, USA, [5]NASA Marshall Space Flight Center, Huntsville, AL, USA, [6]The Blackett Laboratory, Department of physics, Imperial College London, London, UK, [7]Laboratory for Atmospheric and Space Physics, University of Colorado Boulder, Boulder, CO, USA, [8]Physics Department and Space Science Center, University of New Hamsphire, Durham, NH, USA, [9]Department of Physics, University of Texas at San Antonio, San Antonio, TX, USA, [10]Space Research Institute, Russian Academy of Sciences, Moscow, Russia, [11]Institute of Space and Astronautical Science, JAXA, Sagamihara, Japan, [12]Swedish Institute of Space Physics, Uppsala, Sweden, [13]Laboratoire de Physique des Plasmas, CNRS/Ecole Polytechnique/Sorbonne Université/Université Paris-Sud/Observatoire de Paris, Paris, France, [14]Space Research Institute, Graz, Austria, [15]Space Sciences Laboratory, University of California, Berkeley, CA, USA, [16]Institute of Geophysics, Earth, Planetary, and Space Sciences, University of California, Los Angeles, CA, USA, [17]Astronomy Department, University of Maryland, College Park, MD, USA, [18]Graduate School of Science, Osaka University, Toyonaka, Japan

Abstract We present a new method for determining the main relevant features of the local magnetic field configuration, based entirely on the knowledge of the magnetic field gradient four-spacecraft measurements. The method, named "magnetic configuration analysis" (MCA), estimates the spatial scales on which the magnetic field varies locally. While it directly derives from the well-known magnetic directional derivative and magnetic rotational analysis procedures (Shi et al., 2005, htpps://doi.org/10.1029/2005GL022454; Shen et al., 2007, https://doi.org/10.1029/2005JA011584), MCA was specifically designed to address the actual magnetic field geometry. By applying MCA to multispacecraft data from the Magnetospheric Multiscale (MMS) satellites, we perform both case and statistical analyses of local magnetic field shape and dimensionality at very high cadence and small scales. We apply this technique to different near-Earth environments and define a classification scheme for the type of configuration observed. While our case studies allow us to benchmark the method with those used in past works, our statistical analysis unveils the typical shape of magnetic configurations and their statistical distributions. We show that small-scale magnetic configurations are generally elongated, displaying forms of cigar and blade shapes, but occasionally being planar in shape like thin pancakes (mostly inside current sheets). Magnetic configurations, however, rarely show isotropy in their magnetic variance. The planar nature of magnetic configurations and, most importantly, their scale lengths strongly depend on the plasma β parameter. Finally, the most invariant direction is statistically aligned with the electric current, reminiscent of the importance of electromagnetic forces in shaping the local magnetic configuration.

1. Introduction

In a magnetized plasma the local configuration of the magnetic field plays a key role to determine the system's dynamics at all scales, in particular, by controlling the evolution of large structures, regulating how waves propagate and feeding most of the instabilities that can be excited. Therefore, when studying the dynamics of near-Earth plasmas (e.g., solar-wind, magnetosheath, and magnetosphere), it is of fundamental importance to understand how the magnetic field is locally shaped.

In the past, much of the research in this direction has proceeded by identifying and characterizing specific magnetic field structures on the basis of known models. Flux ropes, current sheets, and X and O lines are among such structures that have been investigated theoretically by means of large-scale numerical simulations and analytical models, as well as experimentally, since spacecraft data have confirmed their presence in the near-Earth environment. In this context, multispacecraft missions with small-scale satellite formations, such as Cluster (Escoubet et al., 1997), THEMIS (Time History of Events and Macroscale Interactions during Substorms, Angelopoulos, 2008), and MMS (Magnetospheric Multiscale mission, Burch et al., 2016) have been of the utmost importance by giving the possibility to sample the same structure at different locations simultaneously, thereby allowing one to obtain a "three-dimensional" (or—better—more than one-dimensional) view of the plasma structure at a given time.

The use of gradient-based methods to analyze multispacecraft data and obtain some idea of the local magnetic field configuration has been widely discussed in literature. Recently, for instance, Shen et al. (2003) undertook the study of magnetic field curvature, focusing mainly on understanding the neutral sheet in the magnetotail but developing general tools in this process. A different way to deal with magnetic field configuration is the magnetic directional derivative (MDD) procedure presented in Shi et al. (2005). In spite of its widespread application as a frame-determining method, MDD has been repeatedly used as starting point for studies of local magnetic configurations (Denton et al., 2010, 2012, 2016, 2018; Rezeau et al., 2018; Shi et al., 2006). An alternative to this method, called magnetic rotational analysis (MRA), comes from the generalization of the Shen et al. (2003) curvature study and can be found in Shen et al. (2007). The main difference between MRA and MDD is that in MRA only the local magnetic field direction (normalized magnetic field) is considered, so that the parameters provided by this method are relative to the local magnetic field geometry, or shaping, independent of the magnetic field intensity.

In this work, we aim at investigating how the magnetic field is configured on the tens-of-kilometers scale in the magnetosphere, magnetosheath, and near-Earth solar wind plasma environments. We analyze local magnetic field configurations by performing the so-called "magnetic configuration analysis" (MCA), a method newly developed here which consists in a slight modification of the MDD and MRA techniques. In the present paper, we show that high-resolution data and the small spacecraft separation of the MMS mission can be successfully used to determine local magnetic configurations by evaluating small-scale variations of the magnetic field in the three spatial directions. In order to prove the validity of our results, we perform two different studies. First, we test MCA on long and continuous low-resolution measurements (fast survey data) to obtain statistics of local configurations; second, we focus on short intervals sampled at high resolution (burst mode data) when MMS encounters "specific" plasma structures. The pictures of magnetic field configuration emerging in both cases agree with previous works and validate a number of general assumptions regarding typical local configurations of the magnetic field in the near-Earth plasma environments.

The paper is organized as follows. In section 2 we describe the techniques developed to measure the local shaping of the magnetic field and present some remarks on how these methods are exploited in our analysis. In section 3 we summarize the main features and capabilities of the MMS instrumentation. Data analysis is presented in section 4 (high-resolution burst data for selected events) and section 5 (low resolution fast survey data in a statistical approach). We discuss the results in section 6; conclusions are drawn in section 7.

2. Materials and Methods: Techniques to Sample Local Magnetic Configurations

One of the most used techniques to measure local configurations of the magnetic field **B** is the MDD method developed by Shi et al. (2005). The idea behind MDD is that all relevant information on the local magnetic field configuration is contained in the square of the directional derivatives of **B** at any given point in space. By identifying a generic direction by the unit vector **e**, the square of the directional derivative along **e** is given by

$$I_{\mathrm{MDD}}(\boldsymbol{e}) := [\boldsymbol{e}\cdot\nabla\boldsymbol{B}]^2 = \boldsymbol{e}\cdot\nabla\boldsymbol{B}\cdot[\nabla\boldsymbol{B}]^T\cdot\boldsymbol{e}^T =: \boldsymbol{e}\cdot\boldsymbol{L}\cdot\boldsymbol{e}^T$$

where the superscript "T" indicates the transpose (for either vectors or matrices). Since the last equality in the previous formula relates this direction-dependent quantity $I_{\mathrm{MDD}}(\mathbf{e})$ to a direction-independent tensor field **L** (defined as the scalar product between the tensor gradient of **B** and this same tensor, transposed),

then according to the MDD paradigm **L** carries all information about local magnetic configurations through our system.

However, a weak point of the MDD method in determining the local configuration of the magnetic field is its dependence on the local intensity of the magnetic field and not only on the magnetic field local shape. For example, let us assume we perform MDD on some magnetic configuration, then change (globally) the intensity of **B** and perform MDD again. While the MDD outcome (that is, **L**) has changed between these two calculations, what we intend as "magnetic configuration" in the two cases is exactly the same. Therefore, MDD is not the best-suited tool for studies focusing on the sole local magnetic field configuration.

To investigate magnetic configurations but avoid obtaining a result, which depends on the local field intensity, an alternative to MDD is to carry out a MDD-like analysis on the normalized magnetic field $\mathbf{b} := \mathbf{B}/B$. This procedure, introduced by Shen et al. (2007), is known as "MRA". This method is based on the variation of **b** along the **e** direction:

$$I_{\mathrm{MRA}}(\boldsymbol{e}) := [\boldsymbol{e}\cdot\nabla\boldsymbol{b}]^2 = \boldsymbol{e}\cdot\nabla\boldsymbol{b}\cdot[\nabla\boldsymbol{b}]^T\cdot\boldsymbol{e}^T =: \boldsymbol{e}\cdot\boldsymbol{S}\cdot\boldsymbol{e}^T$$

whose square root, in the nomenclature of Shen et al., is called "magnetic rotation rate along **e**". Similar to **L** in MDD, in MRA the sole tensor field **S** defined above carries all information related to all possible "rotation rates" in all directions for each point in space and, therefore, about the local magnetic configuration as determined by MRA. While not depending on local magnetic field intensity, however, MRA cannot describe the fully three-dimensional nature of magnetic configurations. This can be shown once considered that the **b** field (on which MRA is built) has only two degrees of freedom: because of this the tensor **S** is degenerate, that is, its determinant must be zero and therefore one of the MRA eigenvalues is always null (as detailed in Appendix A). In conclusion, by construction **S** would describe a three-dimensional configuration only by two characteristic lengths. Therefore, neither MRA is well suited for the analysis of three-dimensional shapes as we intend to perform here.

The approach we propose to investigate local three-dimensional magnetic field configurations, while avoiding the limitations of both MDD and MRA, is to consider a "normalized MDD" method where instead of considering **L** or **S** we focus on the tensor **N** defined by

$$\mathbf{N} := [\nabla\boldsymbol{B}]\cdot[\nabla\boldsymbol{B}]^T/B^2$$

with B indicating local intensity of the magnetic field. Since **N** does not change under rescaling of **B** (thanks to the factor B appearing at the denominator in the definition of **N**) nor it is forcedly degenerate, it does contain all information that we deem relevant for describing any local magnetic configuration. We shall refer to the procedure of sampling magnetic configurations by the **N** tensor field with the name "MCA."

From this point to the end of this section we will discuss which quantities one can define so as to best express all information contained inside **N** that—we remind—describes linear variation of the magnetic field between tens-of-kilometers and hundreds-of-kilometers scales (see Text S1 in the supporting information).

Since **N** is symmetric, its value at each position is totally determined by its three "proper directions" (eigenvectors, adimensional) and "proper values" (eigenvalues, dimensionally these are inverses of lengths):

$\sigma_{\max}$	maximum eigenvalue	$\pm\mathbf{e}_{\max}$	direction of maximum eigenvector
σ_{med}	intermediate eigenvalue	$\pm\mathbf{e}_{\mathrm{med}}$	direction of intermediate eigenvector
$\sigma_{\min}$	minimum eigenvalue	$\pm\mathbf{e}_{\min}$	direction of minimum eigenvector

A somewhat intuitive way to deal with the information contained in these quantities is to visualize the **N** tensor field as a set of ellipsoids, one for each point in space, constructed so that ellipsoid's axes are everywhere aligned along the local eigenvectors, the axes' lengths inversely proportional to the square roots of the corresponding eigenvalues. This representation of **N** as set of "variance ellipsoids" makes it possible to obtain a synthetic picture of the variations of **B** in different directions. In particular, since the linear

approximation of the magnetic field differs by the same angle along all axes of each ellipsoid, one concludes that the rotation ellipsoid will be stretched the most along those directions in which rotation rates are the least, that is, where the field is "most uniform" (see Figure 1a). Given the evident character of the ellipsoid depiction of **N**, from now on we shall see the variance ellipsoids as equivalent to local field configurations determined by MCA.

The most natural way we found to classify local magnetic configurations consists in following past works that aimed at characterizing Cluster spacecraft tetrahedral shapes (see Robert et al., 1998, and references therein). Keeping this model in mind, we recognize that information provided by MCA can be best organized in two parts, one concerning the scale and one the shape of local rotation ellipsoids. While local scale can be well represented by $1/\sqrt{\sigma_{\max}}$, that is, the smallest length in the magnetic configuration, to express the ellipsoid's shape, it is useful to define the following two parameters:

$$\begin{array}{ll} \text{elongation} & \mathscr{E} := 1 - \sqrt{\sigma_{\min}/\sigma_{\text{med}}} \\ \text{planarity} & \mathscr{P} := 1 - \sqrt{\sigma_{\text{med}}/\sigma_{\max}} \end{array}$$

These parameters measure the tendency of the local rotation ellipsoid to squeeze toward some one-dimensional elongated form ($\mathscr{E} \to 1$) or to flatten into a quasi-two-dimensional surface ($\mathscr{P} \to 1$). Therefore, the (local) shaping of **B** may be represented by a point in the $\mathscr{E}$-$\mathscr{P}$ parameter space (Figure 1b). We also decide to classify the local shape of **B** by picking up the terminology used for spacecraft tetrahedra: "pseudo-spheres" (low $\mathscr{E}$, low $\mathscr{P}$), "cigars" (high $\mathscr{E}$, low $\mathscr{P}$), "pancakes" (high $\mathscr{P}$, low $\mathscr{E}$), and "knife blades" (high $\mathscr{E}$, high $\mathscr{P}$) — the more generic "potato" (intermediate $\mathscr{E}$ and $\mathscr{P}$) being left out of our discussions for the sake of simplicity (for a visual representation of this classification, see Figure 1b).

This shape classification naturally leads to the possibility of recognizing local approximate "dimensionalities" for the magnetic field configuration. For example, where **B** displays a pancake shape, we know that its variation in one direction is much more pronounced than in the other two, and thus, the local magnetic environment is quasi one-dimensional. Conversely, finding a cigar shape suggests that variations in **B** along the longest of the ellipsoid's axes can be neglected with respect to those in the directions perpendicular to it, and thus, the local magnetic structure can be thought of as two-dimensional. Note that the axes of our characteristic ellipsoids have been defined as the characteristic variation lengths of the magnetic field, and therefore, "dimensionalities" are determined by the shortest rather than the longest of the ellipsoid's scales.

These considerations on shape and dimensionality are very important also when considering the orientation of rotation ellipsoids, that is, the direction of the local **N** eigenvectors. We recall that eigenvector directions are well defined only when the corresponding eigenvalues are well separated from one another (that is, when all eigenvalues are either much greater or much smaller than all others). This condition is equivalent to the request that parameters P and E must be not null, and therefore, we understand that the only well-defined directions are the longest axis in cigars and knife blades and the shortest axis in knife blades and pancakes. So, whenever we observe a series of "knife blade" and "pancake" shapes through some data interval, there $\mathbf{e}_{\max}$ provides a clear maximum angular variance direction, while only through intervals consisting of knife blades and cigars $\mathbf{e}_{\min}$ determines a clear direction of approximate invariance.

When dealing with proper variance directions, there we need some orientation criterion in order to present the directions of variation ellipsoid axes by unitary vectors. A somewhat "natural" prescription could be to orient each unitary vector to minimize the angle between it and some other unitary vector taken as reference. This criterion, however, can allow small changes in the original ellipsoid to provoke sudden 180° reversals in the resulting oriented unitary vectors. To avoid this, we exploit the fact that we are dealing with time series, and thus, we just require the angle between two consecutive eigenvectors to be minimal. Once the orientation of the first vector has been arbitrarily selected, this prescription avoids sudden 180° reversals, therefore ensuring a "smooth transition" between consecutive unitary vectors.

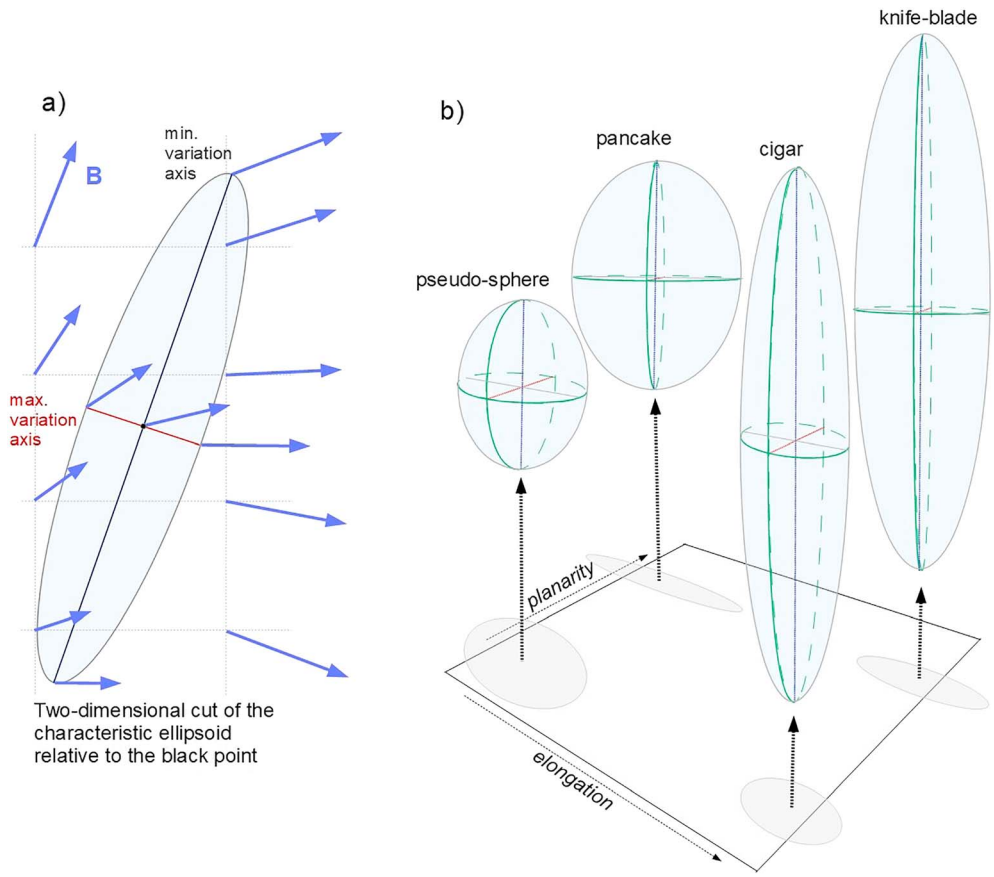

Figure 1. (a) A sketch showing how the characteristic variation ellipsoid relative to the black point would appear, given the local magnetic configuration suggested with blue arrows. Differences between the magnetic field at the center of the ellipsoid (black point) and that at the endpoints of its axes are the same for each of the axes. Note that for simplicity we have made the choice of drawing only a two-dimensional plane cut of the three-dimensional field and ellipsoid. (b) Variation ellipsoid in the standard configurations of pancake, knife-blade, pseudo-sphere, and cigar, with the maximum and minimum variation axes highlighted in red and blue, respectively. Shadows have been added on the bottom plane for clarity. For a pancake shape (low $\mathscr{E}$, high $\mathscr{P}$) the maximum and intermediate rotation lengths are nearly equal, while in a "cigar" (high $\mathscr{E}$, low $\mathscr{P}$), it is the intermediate and minimum ones that are similar. The case of well-separated lengths (high $\mathscr{E}$, high $\mathscr{P}$) falls under the denomination of "knife-blade," while "pseudo-sphere" is used for three similar axes (low $\mathscr{E}$, low $\mathscr{P}$).

3. MMS Instrumentation and Multispacecraft Data

The MMS mission (Burch et al., 2016) consists of four identical satellites flying in close formation (the inter-spacecraft distance is on the order of a few tens of kilometers) along elongated, nearly equatorial orbits passing through the Earth's magnetopause and its surroundings. Each of the four spacecraft is equipped to provide measurements of plasma properties, giving the possibility to obtain linear estimates for gradients of all recorded quantities (Chanteur, 1998) and therefore, to perform analyses such as MCA. Despite the extremely high sampling frequencies, telemetry limitations imply that only some percentage of the data can be downloaded at the highest resolution ("burst mode"), all the rest being available just as low-resolution measurements ("survey mode"). In order to carry on structure-specific analyses (section 4) we seek for "burst" data intervals, while to get a statistical picture of near-Earth plasma (section 5), we exploit "survey" measurements.

In particular, when performing our analysis on MMS data, we exploit position measurements (Tooley et al., 2015) interpolated onto the magnetic field recorded by the FluxGate Magnetometer (FGM, Russell et al., 2016), sampled with an accuracy of 0.1 nT at 8 Hz for "slow survey" mode intervals, at 16 Hz for "fast survey" mode and at 128 Hz for "burst" mode. Given these instrumental accuracies, the precision of MCA results has been tested by a bootstrap-like procedure, that is by confronting values of MCA quantities found for some interval with those obtained on the very same input data but perturbed randomly inside their uncertainty

intervals (see Figures S1 and S2 in the supporting information). In all cases considered, these tests have shown that a simple evaluation of the minimal resoluble eigenvalue is given by

$$\min_{res} \sigma = \frac{[\delta B]^2}{\ell^2 B^2}$$

where δB is the accuracy of the FGM instrument, B is the local mean intensity of the magnetic field, and ℓ stands for spacecraft separation. Moreover, it can also be shown that the capability of the MMS swarm to spatially resolve magnetic configurations does not change when using "survey" or "burst" data (see Text S1 for extended discussion), and therefore, all magnetic configuration analyses carried out in the two following sections are totally consistent with each other.

Particle data used in this paper (density, bulk velocity, and plasma pressures, used for figures and the statistical analysis) are obtained from the Fast Plasma Investigation (FPI; Pollock et al., 2016).

4. Characteristic Shapes and Dimensionalities Inside Flux Ropes and Current Sheets

We now illustrate the results of performing MCA on spacecraft data for specific crossings of flux ropes and current sheets, similar to the case studies performed by Shen et al. (2007) when introducing the MRA method or Shi et al. (2005) when presenting the MDD technique. By making use of MMS high-resolution data (instead of Cluster measurements exploited in the two studies just cited), here we are able to investigate the magnetic configurations at the tens-of-kilometers scale on the dayside magnetopause, much smaller than the 1,000-km-scale features examined by Shen et al. (2007) with Cluster in the magnetotail, for instance.

In Figure 2 we present a dataset containing two ion-scale flux-ropes, which were observed within a reconnection exhaust at the magnetopause, as discussed by Eastwood et al. (2016). The magnetosphere, sampled at the beginning of the interval, is recognizable thanks to clearly positive values of B_z in geocentric solar equatorial coordinates; the magnetosheath appears at the end of the interval (negative B_z). The flux ropes were identified, thanks to bipolar variations in the B_x and B_z magnetic field components (see panel a) and peaks in both magnetic and total pressures (panel d). The crossings of the flux ropes are identified in Figure 2 by the 2-s shadings with labels "FR 1" and "FR 2" (FR for "flux rope"). We also show the FPI current (panel b) and the ion velocity (panel c), for context.

In the last four panels we display MCA results: the three eigenvalues (panel e), the two shape parameters E and P (panel f), the direction of $\mathbf{e}_{\max}$ (panel g), and that of $\mathbf{e}_{\min}$ (panel h) both expressed as unitary vectors. All MCA data presented here are presented using a 10-point moving window average, in order to smooth out some minor spiky oscillations. The thin, dark red line in the eigenvalue plot represents an expected lower accuracy limit that is analytically derived using an absolute magnetic field accuracy of 0.1 nT (see section 3 for the exact formula). Since the least MCA eigenvalue lays usually close or even below this threshold, in general, we would not expect it to bear precise information — a limitation that is reflected therefore also in the values retrieved for the E parameter, but not necessarily in $\mathbf{e}_{\min}$ since this eigenvector can be determined by vector product of the remaining two.

Aware of these caveats, let us yet compare MCA performance to that of known analyses on this event. In particular, one would expect $\mathbf{e}_{\min}$ to identify the axis direction of flux ropes (as explained in section 2). This is indeed what we observe when investigating statistically the angle between the axis obtained in Eastwood et al. (2016) and the minimal MCA eigenvector direction around 13:04:34 UT (when the spacecraft was passing closest to the flux-rope core, as highlighted by the shading in the figure). Indeed, the angle distribution shows a sharp peak at 15° (the so-called "statistical mode" value), and for 50% of the data points in the interval considered this same angle is below 20° (for details on the cosine statistics, see Appendix B).

In Figure 3 we plot the same quantities as in Fig 2 for a crossing of a current sheet embedded within a larger-scale compressive structure. While a first glance at the quantities in panels (a) to (d) might suggest that this event is similar to the previous one (note in particular similarities in the pressures), strong differences in the plasma properties before and after the magnetic field peak led Kacem et al. (2018) to identify this structure as the collision of two separate flux tubes. The thin current sheet in the middle of the event around 14:16:41 UT

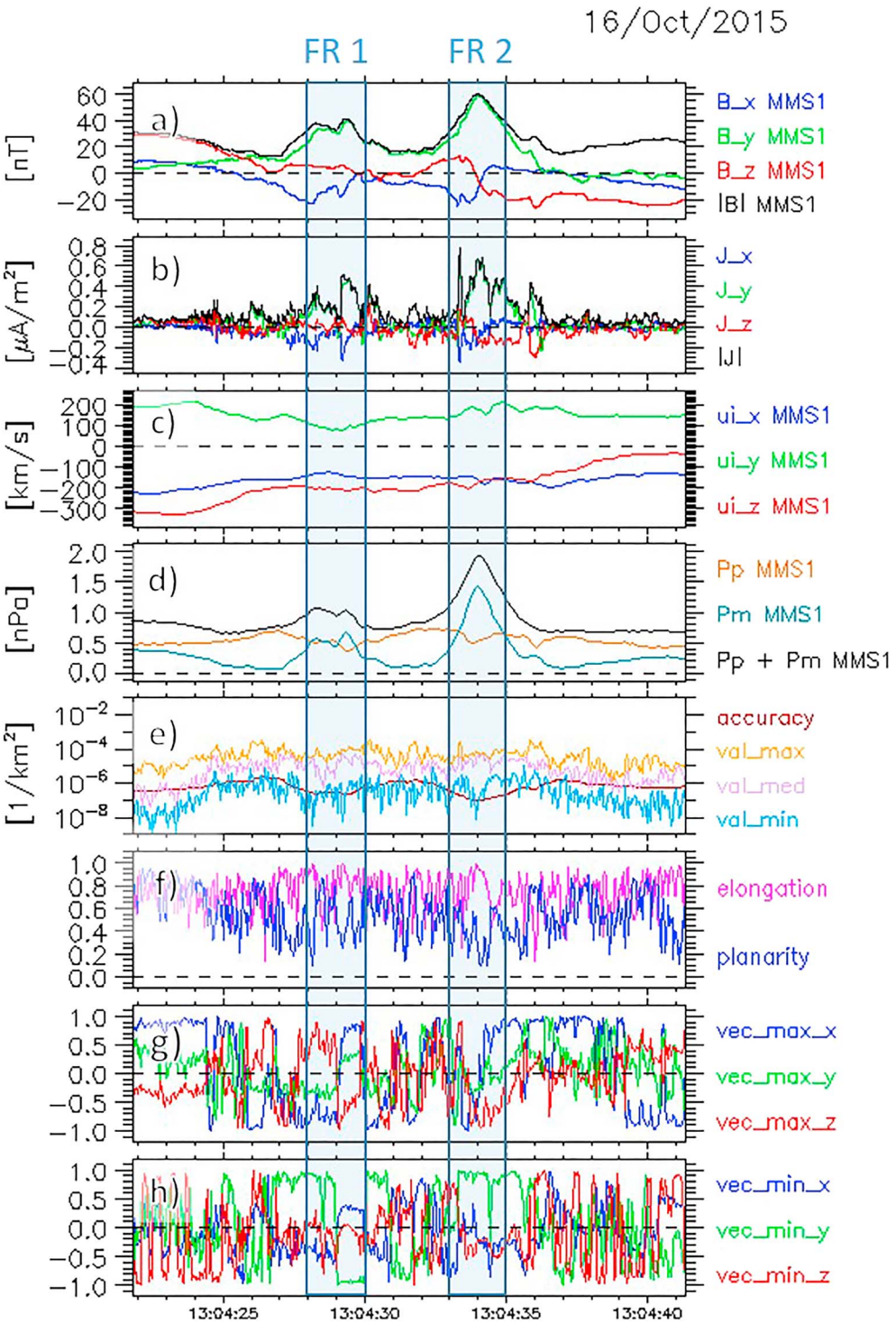

Figure 2. Data recorded by MMS2 between 13:04:20 and 13:04:45 UT on 16 October 2015, and results of the (four spacecraft) magnetic configuration analysis (MCA) analysis on the same data interval. This event was studied in Eastwood et al. (2016) that identifies the two flux rope crossings highlighted by the shaded strips, labeled "FR 1" and "FR 2." The four upper panels show characteristic plasma quantities: (a) magnetic field, (b) current from particle measurements, (c) bulk ion flow (in geocentric solar equatorial coordinates), and (d) the three plasma "pressures" (thermal, magnetic and total). The four lower panels display MCA results: (e) eigenvalues, (f) shape parameters (E and P), and (g–h) the three components of the maximal and minimal normalized eigenvectors, respectively. The dark red line in the eigenvalue plot (panel e) estimates the expected accuracy threshold presented in section 3. Notice that the "least variance" direction given by $\pm\mathbf{e}_{\min}$ is well aligned with the flux rope axis estimated by Eastwood et al. (2016) through all the traversal of the second flux rope, highlighted by the shading. Spatial scales of flux ropes do not stand out as markedly different from those of the surrounding plasma, as indicated by the generally constant behavior of MCA eigenvalues.

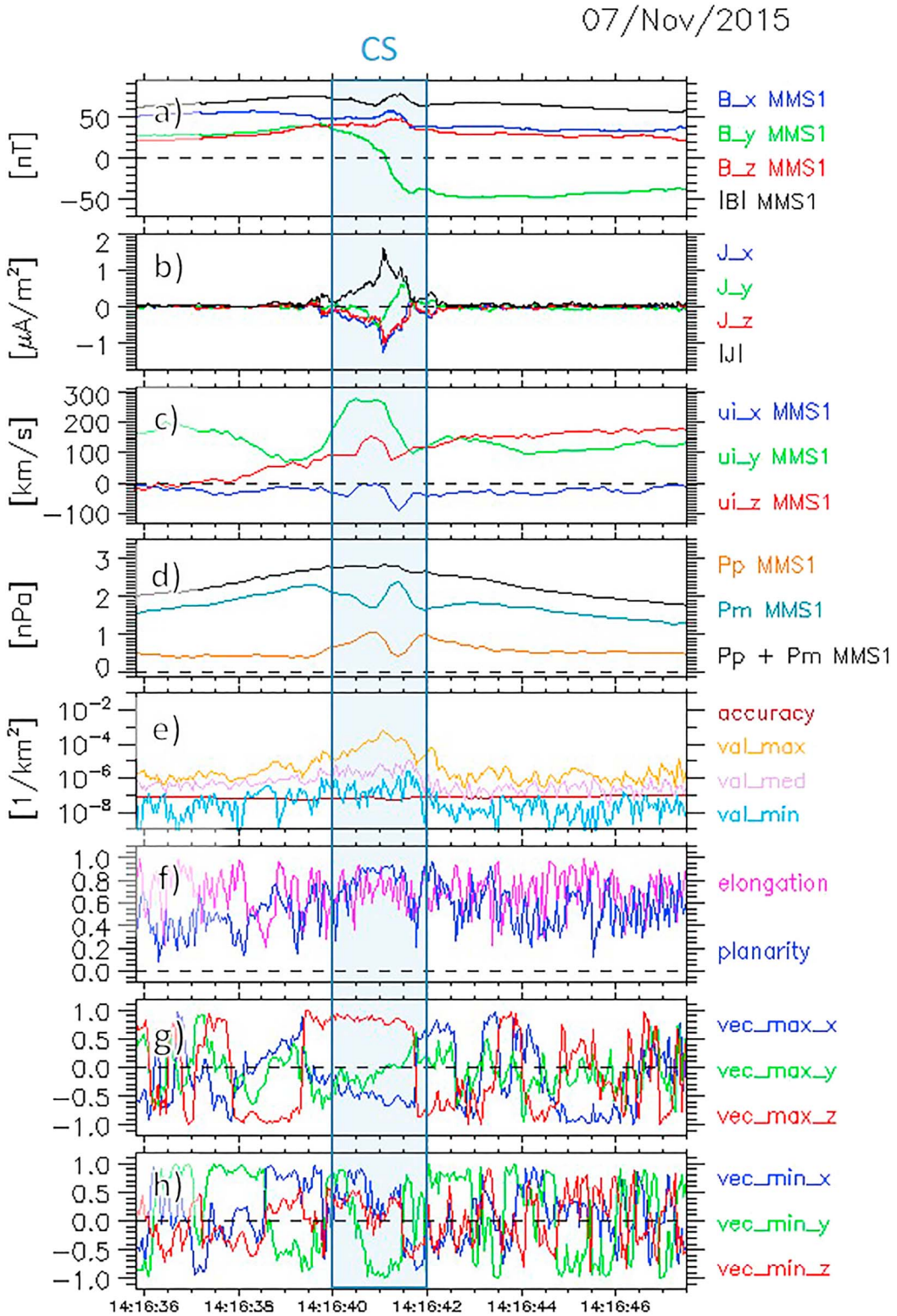

Figure 3. (a–h) Overview of MMS2 observations and magnetic configuration analysis (MCA) results between 14:16:25 and 14:16:55 UT on 7 November 2015. This event was studied in Kacem et al. (2018) and Zhou et al. (2018), which both identified the shaded time interval labeled "CS" as a current sheet crossing. All quantities presented in the panels are the same as in Figure 2. The peaking of σ_{max} at the time of the highlighted interval (see panel e) indicates that one of the characteristic scales in the local magnetic field configuration is much lower inside the current sheet than in its surroundings. The direction in which **B** develops its smallest variation scale, indicated by $\pm\mathbf{e}_{max}$ (see panel g), is consistent with the one found via MVA as reported by Kacem et al. (2018) during all the entire, highlighted current sheet traversal.

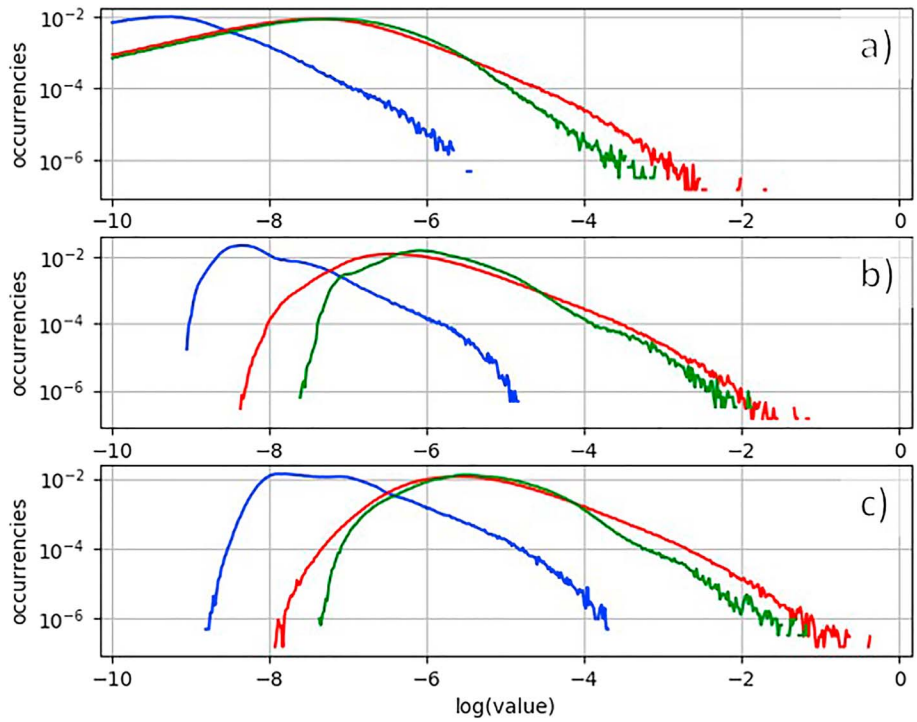

Figure 4. Normalized occurrence distribution of magnetic configuration analysis eigenvalues: (a) $\sigma_{\min}$, (b) σ_{med}, and (c) $\sigma_{\max}$. The three colored lines indicate statistics corresponding to each of the three plasma environments sampled: blue for the magnetosphere, red for the magnetosheath, and green for the solar wind. From this statistics it appears that in general the smallest scales are found in the magnetosheath and the largest in the magnetosphere.

arises from the interaction of the flux tubes (the shaded 2-s interval labeled "CS") and was demonstrated to be reconnecting (in Figure 3 this can be seen in particular by looking at the ion flow, consistent with a reconnection exhaust). A thorough study of this event can be found also in Zhou et al. (2018).

Again, here MCA can be tested by comparing directions individuated by MCA eigenvalues inside the current sheet with known results, and again, MCA is found coherent with expectations. Indeed, while $\mathbf{e}_{\min}$ oscillates (note that the more elongation differs from one, the worst the minimum rotation rate is determined; see section 2), $\mathbf{e}_{\max}$ points nearly along the current sheet normal calculated by Kacem et al. (2018). Statistics on the angle between the normal from timing estimate and MCA show a distribution sharply peaked at 10° (statistical mode), with values falling below 12° for 50% of the data points (again, see Appendix B for details on this kind of statistics).

Having ascertained that MCA preforms consistently with known analysis methods, let us now focus on its results regarding local shapes and scales of magnetic configuration. In the first event examined, especially the second flux rope shows a tendency for the magnetic field to be very elongated with little planarity (Figure 1e). Apart from this, however, not much stands out during the whole interval, meaning that the detectable local configuration of the magnetic field does not change much between the inside of these structures and their surroundings. Passing on the second event, we note that in spite of a very similar behavior in the usual average plasma parameters, results from MCA differ greatly between this current sheet traversal (panels (e) to (h) of Figure 3) and the flux rope crossings discussed previously (panels (e) to (h) of Figure 2). In particular, in correspondence with the current sheet traversal studied by Kacem et al. (2018) and Zhou et al. (2018), we observe that both $\sigma_{\max}$ and P rise, thus indicating that magnetic configurations inside current sheets display smaller scale and more planar shapes than in the surrounding environment. In other words, known magnetic structures might be associated to some average configuration signature that one obtains as mean of MCA eigenvalue/shape parameter values.

These analyses have been replicated on a number of other events containing current sheets or flux ropes previously studied in the literature, as well as on crossings of magnetic holes (see Figures. S3 to S7). Each time

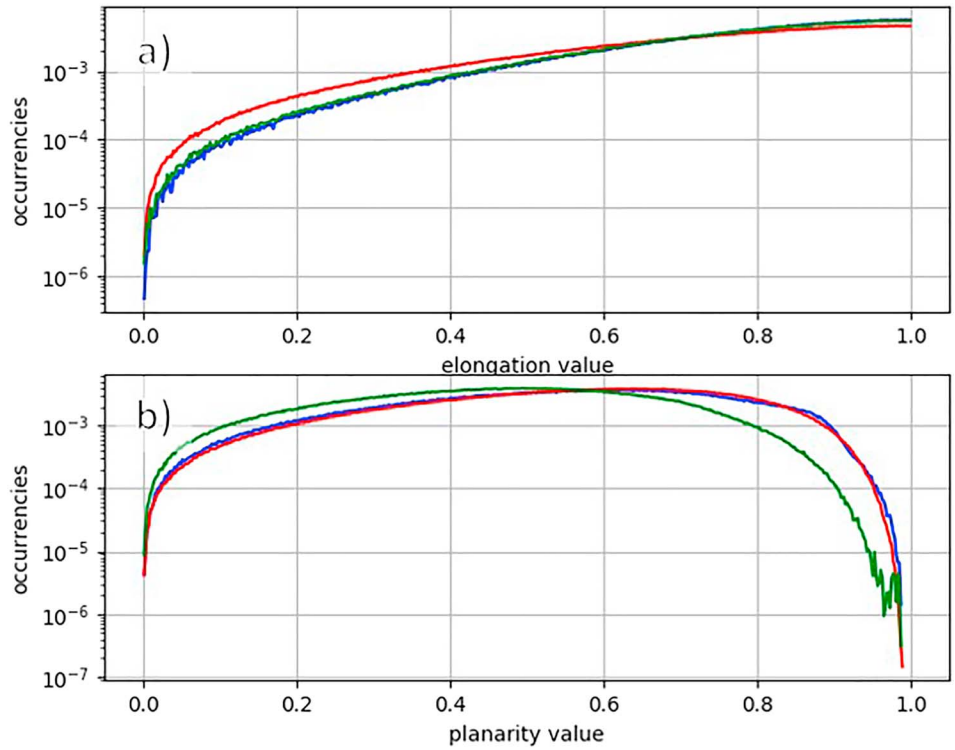

Figure 5. Normalized occurrence distribution of magnetic configuration analysis shape factors: (a) elongation $\mathscr{E}$ and (b) planarity $\mathscr{P}$. As in Figure 4, the three lines indicate statistics corresponding to each of the three plasma environments sampled: blue for the magnetosphere, red for the magnetosheath, and green for the solar wind. From panel (b) we notice that markedly planar configurations are less frequent in the solar wind (notice logarithmic ordinate axis).

we found that MCA behaves consistently with published studies, in particular reproducing for current sheet and flux rope traversals all behaviors described for the two cases just presented. In particular, the direction of MCA eigenvalues agrees with the orientation of the magnetic structure as retrieved by differential timing techniques. Comparison (see Appendix C) has also been carried on between MCA and the MDD and MRA techniques, showing that these three analysis methods in general lead to similar results. These results show that the local configuration determined by MCA is in agreement with the expected shape of the magnetic field for a number of characteristic structures encountered in near-Earth plasmas.

5. Statistical Analyses in Near-Earth Plasma Regions

We investigate here the statistical behavior of MCA parameters for different near-Earth regions: the magnetosphere, the magnetosheath, and the solar wind. Since burst mode data are available only on short data intervals corresponding to the crossing of particular structures (as defined by the Scientist-In-The-Loop (SITL) in charge—see Baker et al., 2016), the MCA method is here only applied to "survey mode" over a larger dataset. Results of this analysis are nonetheless consistent with those obtained on burst mode data (as explained in Text S1). Data selected for this study have been chosen to be representative of the magnetosphere, magnetosheath, and solar wind, all sampled sunward from the terminator during the 5-month period between November 2017 and March 2018 (see Table S1 in the supporting information for the complete list). Magnetosphere, magnetosheath, and the solar wind data intervals were selected based on ion density, ion velocity, and magnetic field values, preferring continuous hour-long takes. Inside the selected data intervals (covering 690 hr overall, 500 in the solar wind, 105 in the magnetosheath, and 85 in the magnetosphere), a further selection has been made by considering only segments in which at least two of the MCA eigenvalues are above the accuracy threshold as defined in section 3 (reducing effective data to 180 hr, 50 in the solar wind, 90 in the magnetosheath, and 35 inside the magnetosphere). Indeed, in many cases $\sigma_{\min}$ is below the threshold set by the prescribed instrumental resolution, corresponding to an elongation larger than what can

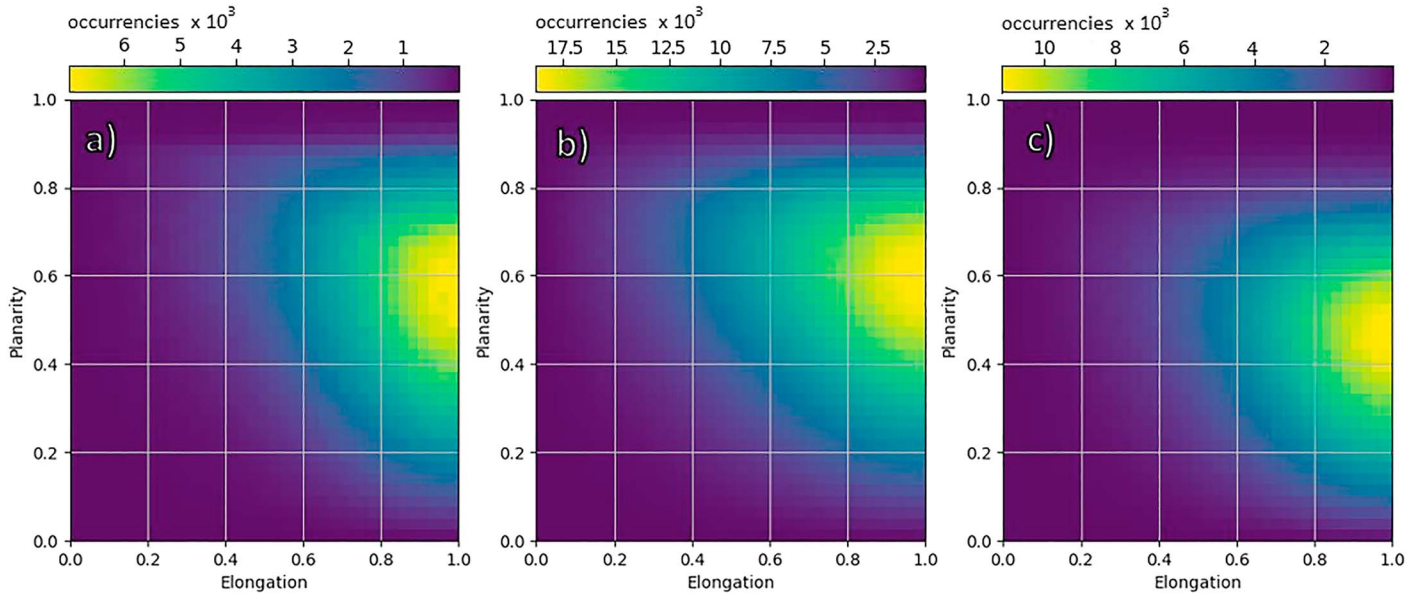

Figure 6. Occurrence distribution of magnetic configuration analysis shapes on the $\mathscr{E}$-$\mathscr{P}$ plane, for the three sampled plasma environments: (a) magnetosphere, (b) magnetosheath, and (c) solar wind. The lighter colors indicate higher number of samples, while the dark blue areas correspond to regions where less samples are present. The three distributions have been retrieved by using the same number of data points for each environment, so to make them easily comparable with each other.

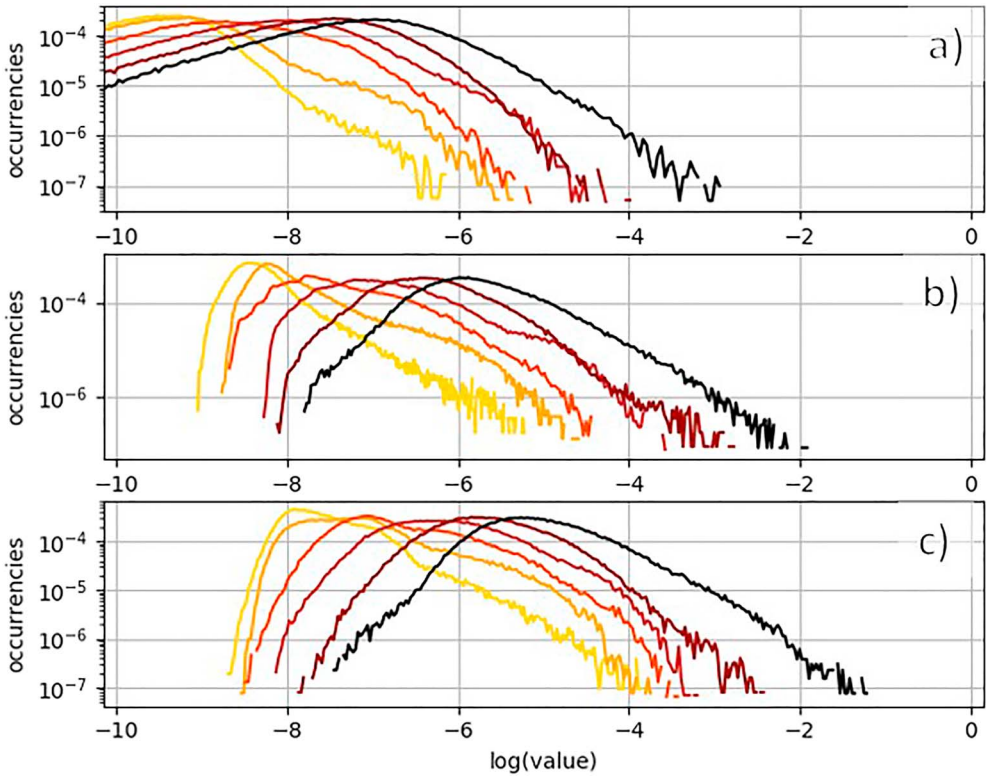

Figure 7. Normalized occurrence distribution of magnetic configuration analysis eigenvalues: (a) σ_{min}, (b) σ_{med}, and (c) σ_{max}. The six lines indicate statistics corresponding to data within the same interval of plasma beta, the six intervals being (0, 0.4), (0.4, 0.75), (0.75, 1.25), (1.25, 2.5), (2.5, 10.0), and all the rest above 10.0. The darker colors are those associated to higher beta values. It appears clearly that the higher the beta, the smaller the characteristic magnetic field scales observed.

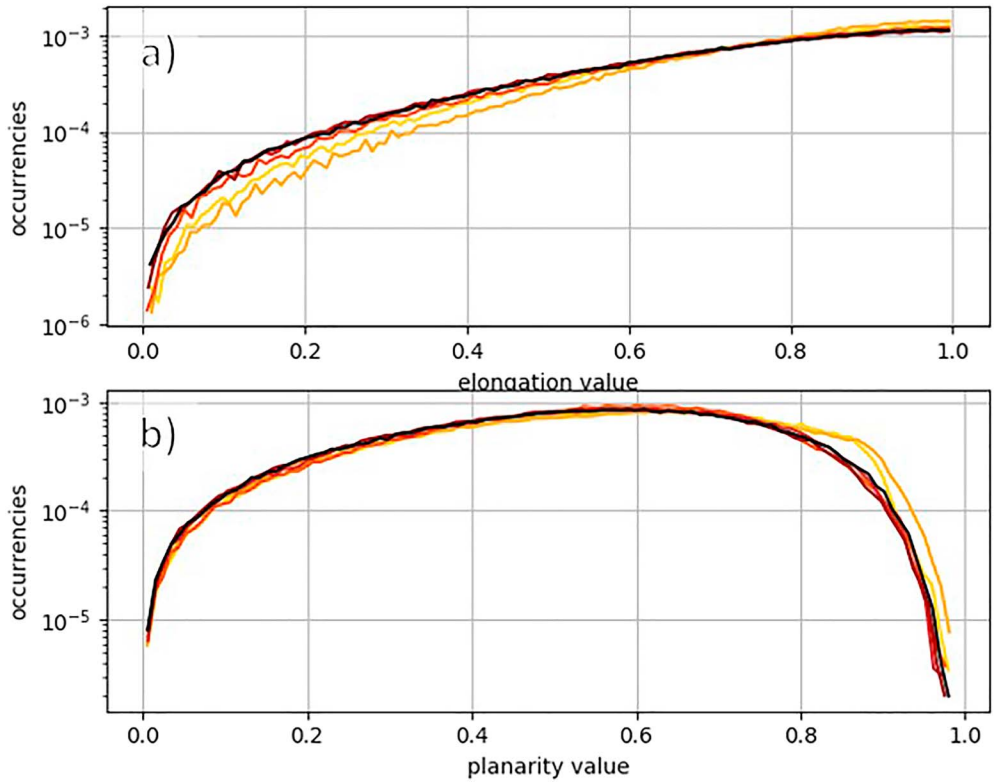

Figure 8. Normalized occurrence distribution of magnetic configuration analysis shape factors: (a) elongation $\mathscr{E}$ and (b) planarity $\mathscr{P}$. As in Figure 8, the five colored lines indicate statistics corresponding to five sets of data grouped together based on plasma beta values. The binning considered is the same exploited for Figure 7. Magnetic configurations show a tendency to develop higher planarities the smaller the local value of beta.

be resolved (more precisely, this happens for around 65% of all time spent in the magnetosheath, and practically always when MMS is traversing the magnetosphere and solar wind). Consequentially, if we were to restrict our statistics on data where all three MCA eigenvalues are properly determined (above the purported threshold), then the results would be not representative of the overall plasma features: this is the reason for which we require that there are at least two well-resolved MCA eigenvalues. Given this selection choice, the only statistical information we can get for $\sigma_{\min}$ is that the largest variation scale of magnetic configurations generally tends to exceed our detection capabilities. In other words, magnetic configurations traversed are usually so elongated in one direction that they can be well approximated as two-dimensional (again, we remind the reader that the spatial scales of the magnetic field considered here are typically between tens of kilometers and thousand kilometers, as detailed in Text S1).

In Figures. 4–6 we present the statistical distribution of MCA parameters, as obtained by analyzing separately the magnetosphere, magnetosheath, and solar wind data segments. In Figure 4 we show the occurrence distributions of the three MCA eigenvalues, different colors standing for different environments. Similarly, in Figure 5 we show the overall occurrences of the P and E values, separately, colors again identifying magnetosphere, magnetosheath, and solar wind statistics. Finally, Figure 6 displays the joint distributions of shape parameters. These show the joint occurrence statistics as spectrograms in the P-E plane, with brighter color being associated here to the most frequent parameter values. Different environments are shown in the three panels.

Of the three environments, the magnetosphere and solar wind show marked differences in their occurrence distributions of MCA eigenvalues, and to some lesser extent regarding local magnetic field shaping. Indeed, the magnetosphere tends to display remarkably smaller MCA eigenvalues than the solar wind, meaning that characteristic variation lengths inside the magnetopause are generally longer than outside. High planarity values are generally missing in the solar wind, indicating that configurations resolved by MMS are more likely planar inside the magnetosphere. In the magnetosheath, we notice two different behaviors

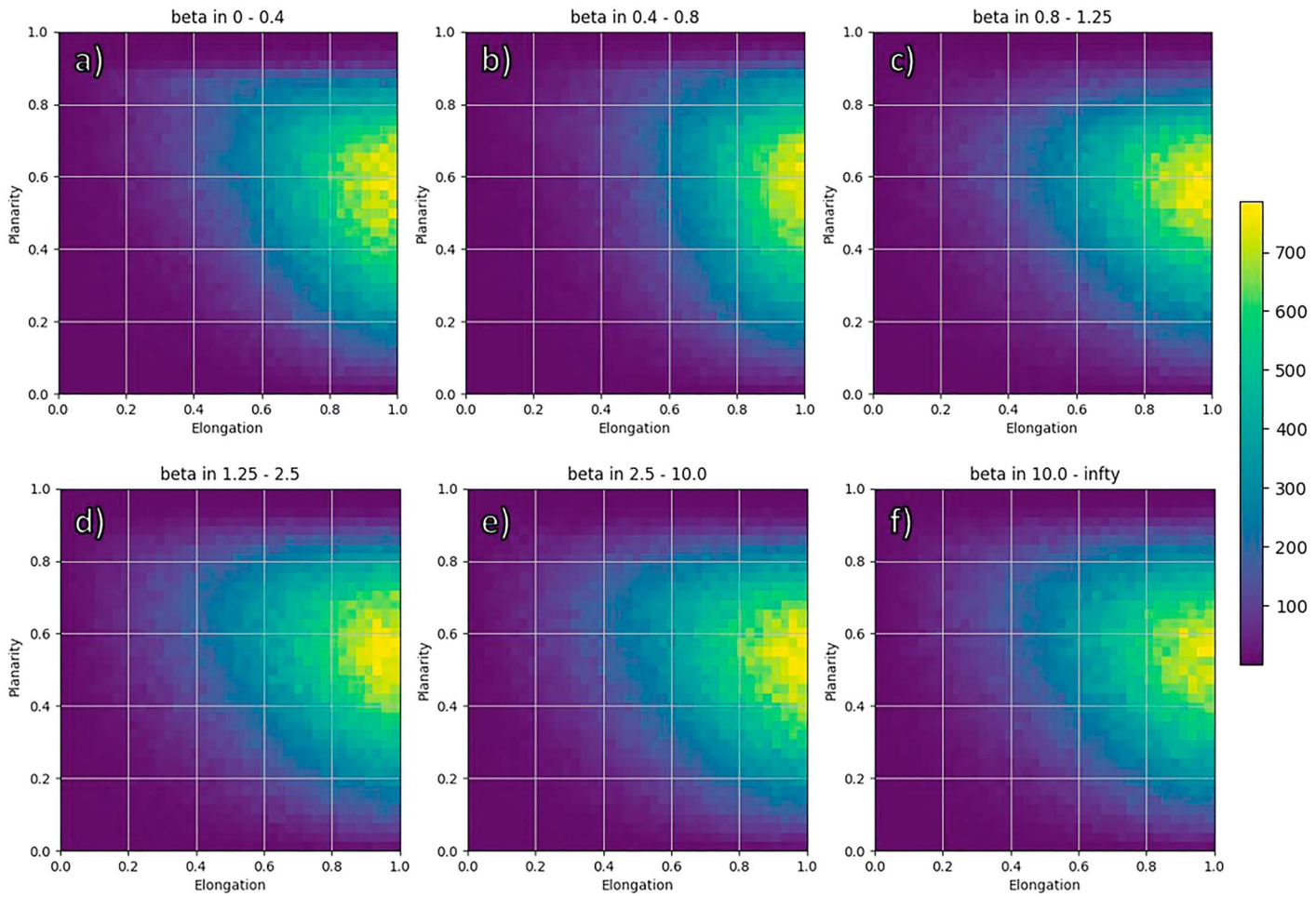

Figure 9. Occurrence distribution for magnetic configuration analysis shapes, similar to Figure 6 but as a function of 6 ranges of plasma beta values. The lighter colors indicate higher number of samples, while the blue areas are the least populated. Again, all six distributions have been drawn out of the same number of data points, so to make them easily comparable with each other. The six plasma beta intervals used in panels (a) to (f) are the same used in Figures. 7 and 8.

depending on whether we look at MCA eigenvalues or if we consider the shape parameters. Indeed, magnetosheath statistics on MCA eigenvalues shows some remarkable similarity to the solar wind, while the distribution of MCA shape parameter is closer to that in the magnetosphere. Overall, the distributions found for the magnetosheath are thus a sort of mix, or average, of the tendencies found on one side in the solar wind and on the other in the magnetosphere.

Clearer trends in eigenvalue and shape factor distributions are observed when the data are merged together and recategorized in terms of the plasma β (ratio of thermal to magnetic pressures). Figures 7–9 show these occurrence distributions as a function of the local plasma β using six ranges of values. Six bins are shown, delimited by plasma β values of 0.0, 0.4, 0.75, 1.25, 2.5, and 10.0 (the sixth bin considers all data taken with plasma β above 10). A random selection of data within these beta intervals has been performed, so that statistics here is carried on an equal number of data for each beta interval (this reduces the overall number of data used in this section to about 10% of the selected points). Note that solar wind data have been left out of this analysis since the ion moments used for calculating the plasma β are deemed not statistically reliable in that region. As anticipated, here a more general trend is present: small β implies larger MCA scales and more planar shapes (knife-blades and pancakes), while high β leads to smaller scales and the appearance of much less planar configurations. We recall here that σ_{min} is typically not well determined, as it is generally below the measurement error estimated analytically for a magnetic field

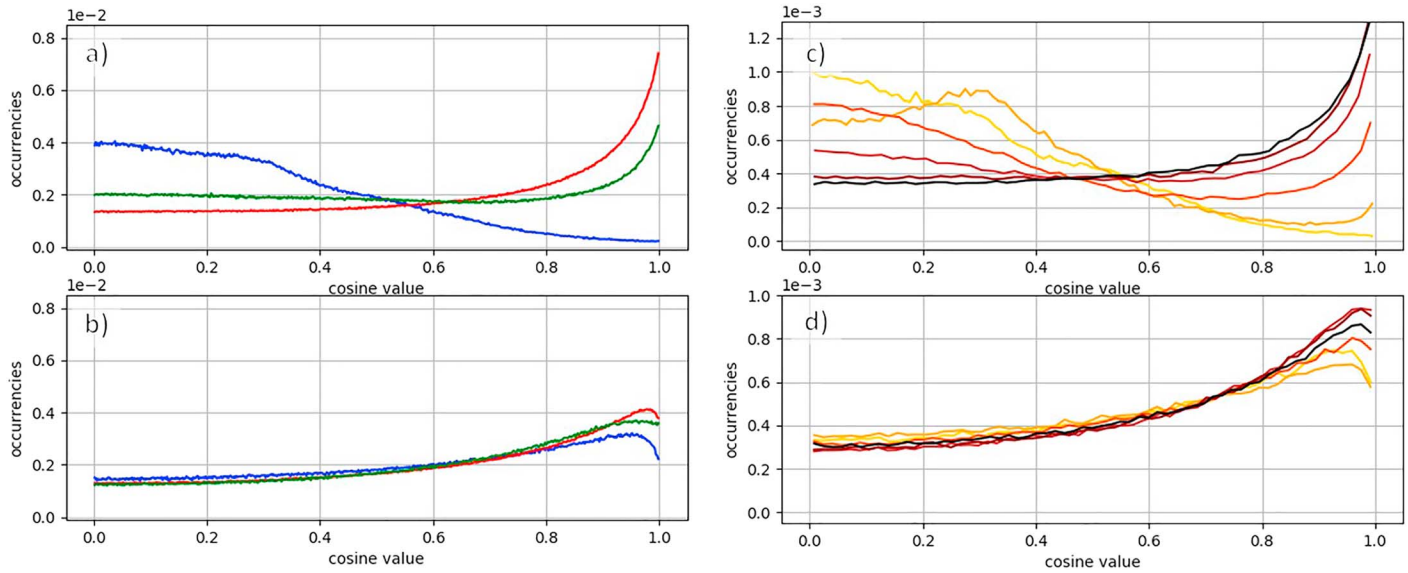

Figure 10. Occurrence distribution of (a and c) $|\mathbf{b}\cdot\mathbf{e}_{\min}|$ and (b and d) $|\mathbf{j}\cdot\mathbf{e}_{\min}|$ normalized on cosine distribution between two random directions. The peak in correspondence of the value one indicates that **b** and **j** tend to align in the same direction as $\mathbf{e}_{\min}$. The colors of the lines indicate occurrence distributions relative to different regions in panels (a) and (b) (blue for the magnetosphere, red for the magnetosheath, and green for the solar wind) and to different beta bins in panels (c) and (d) (from light to dark colors: (0, 0.4), (0.4, 0.75), (0.75, 1.25), (1.25, 2.5), (2.5, 10.0), and all the rest above 10.0).

accuracy of 0.1 nT. This suggests that $\sigma_{\min}$ may often be overestimated, which in turn means that the E may often be underestimated. Therefore, it is likely that the statistical tendency for elongated structures is even more pronounced than what is observed in Figures 5, 6, 8, and 9.

Focusing on MCA eigenvectors, we have studied a possible relationship between their orientation and that of the measured background magnetic field at the same time. In Figure 10, panels (a) and (c), we show the occurrence distribution of $|\mathbf{b}\cdot\mathbf{e}_{\min}|$. Remembering that uncorrelated unitary vectors result in uniform cosine distributions (see Appendix B), we see that the least variance direction (given by $\mathbf{e}_{\min}$) and that of the magnetic field (i.e., **b**) are correlated. Moreover, correlations between these two directions are different in the magnetosphere, magnetosheath, and solar wind. The two vectors are usually parallel to each other in the magnetosheath and solar wind but are mostly perpendicular to each other inside the magnetosphere. Reproducing all the previous procedure with the current density direction $\mathbf{j} := \mathbf{J}/J$ instead of **b**, Figures 10b and 10d are obtained, with the current density obtained using the curlometer technique (see Robert et al., 1998). Again, a correlation is found between the two quantities, meaning that generally **J** and $\mathbf{e}_{\min}$ tend to align (here regardless of the environment sampled).

Alignment of **J** and $\mathbf{e}_{\min}$ can be generally expected for all near-Earth plasma environments, since by definition the derivatives of **B** perpendicular to $\mathbf{e}_{\min}$ are the strongest, and **J** is in good approximation proportional to the curl of **B** (in the physical regimes we study displacement current is negligible). Instead, to explain the various behaviors of **B** we need to recall that in the framework of magnetohydrodynamics, plasma systems are expected to relax in states where **B** and **J** are aligned with each other (the so-called Taylor relaxation, see Taylor, 2000). Now, since we find **B** aligned with **J** in the solar wind and in the magnetosheath, we can conjecture that Taylor relaxation can effectively operate only when no large-scale constraint is imposed. By contrast, the Earth's strong and compressed magnetic field in the dayside magnetosphere might well impede relaxation of the system toward states with **B** and **J** aligned.

6. Discussion and Conclusions

In this paper, we have presented a new method called MCA, an analysis complimentary to the MDD and MRA procedures (Shen et al., 2007; Shi et al., 2005). This technique aims at describing local magnetic field configurations in terms of characteristic variation scales of **B** and differs from MDD and MRA since focuses on **B** as a whole (not just on the unit vector **b**) and is insensitive to re-scaling of this field. Using MCA with

data collected by the MMS mission (Burch et al., 2016), we successfully retrieved the configuration of the local magnetic field in the dayside magnetosphere, the magnetosheath, and the near-Earth solar wind.

Using case studies, we have shown that the results of this procedure are in agreement with those obtained using other techniques for the identification of flux ropes and current sheets, as well as with our expectations concerning the internal magnetic configuration of such structures. In particular, planar magnetic configurations are found inside current sheets where the smallest of the configuration's scale length shrinks (i.e., the thickness of current sheets is generally much smaller than characteristic lengths of the surrounding magnetic structures). Furthermore, a statistical analysis revealed trends in the preferential magnetic configurations observed in the magnetosphere, magnetosheath, and solar wind environments, as well as the correlation of such magnetic configurations with different plasma β values. In particular, with low plasma β values MCA finds the largest characteristic length scales and suggests a more frequent appearance of high planarity values. This might support the idea that magnetically driven plasma dynamics tend to develop naturally into approximately uniform regions separated by current sheets, as it has been suggested in literature (see in particular Parker, 2004).

The same statistical analysis also showed that magnetic configurations are consistently aligned with the mean electric current, that is, that the spatial variance of **B** in the direction parallel to the mean current is significantly lower than in the directions perpendicular to it. The alignment of the most invariant direction with the electric current is reminiscent of the role of electromagnetic forces in shaping the local magnetic field. Alignment of **B** with **J** and the least variance direction, we conjecture, can be accomplished only whenever the absence of large-scale constraints allows the magnetic configuration to relax in states where **J**·**B** is null.

Our findings demonstrate the capabilities and highlight the usefulness of the MCA technique for the analysis of multisatellite data. Information retrieved by performing MCA on satellite data may be of crucial importance in all those studies for which either we make hypotheses on local magnetic configurations or for which we need to estimate characteristic length scales of the system. In the former category we can put all those studies that focus on specific structures (current sheets, flux ropes etc.), and for which MCA could be used both as an additional identification diagnostic and/or to provide characteristic properties (for reference, consider theoretical works such as Zhang et al., 2015, or data-based analyses like Chasapis et al., 2018). In the latter category, we find most studies focus on local frame determination, alongside with all works focusing specifically on characteristic magnetic scales (e.g., Rappazzo, 2015; Rappazzo & Parker, 2013). In all these cases, retrieving and expressing three-dimensional features of the local magnetic field open new possibilities for event-oriented and statistical analyses in near-Earth plasmas.

Appendix A: Demonstrating that det(S) = 0

To demonstrate that the determinant of **S** is always zero, let us describe the normalized magnetic field **b** in terms of the two angles ψ and φ with respect to an arbitrary Cartesian frame:

$$\mathbf{b} = \mathbf{e}_z \cos\psi + \mathbf{e}_x \sin\psi \cos\phi + \mathbf{e}_y \sin\psi \sin\phi$$

Now, for any point in space at least one direction exists that is perpendicular to both ∇ψ and ∇φ: let us indicate that direction (or one of these directions) with the unitary vector $\mathbf{e}_{\mathrm{cst}}$. Since directional derivatives along $\mathbf{e}_{\mathrm{cst}}$ of both ψ and φ are null, also $\mathbf{e}_{\mathrm{cst}}\cdot\nabla\mathbf{b}$ is zero and therefore MRA will always produce $\mathbf{e}_{\mathrm{cst}}$ as an eigenvector with zero eigenvalue. As a consequence, the determinant of **S** is null.

We can give an equivalent demonstration of this result by expressing the gradient of **b** in terms of ψ and φ explicitly (the superscript "*T*" indicating vector transposition):

$$\nabla\mathbf{b} = \left[\mathbf{e}_x \cos\psi\cos\phi + \mathbf{e}_y \cos\psi\sin\phi - \mathbf{e}_z \sin\psi\right][\nabla\psi]^T + \left[-\mathbf{e}_x \cos\psi\sin\phi + \mathbf{e}_y \sin\psi\cos\right][\nabla\phi]^T$$

Therefore, one can easily determine the **S** tensor field to be

$$\mathbf{S} = [\nabla\psi][\nabla\psi]^T + \sin^2(\psi)[\nabla\phi][\nabla\phi]^T$$

From the last expression it follows that det(**S**) is always zero (for an easy demonstration, use the matrix determinant lemma).

Appendix B: Procedures for the Statistical Analysis of Angles

Here we provide more details on the procedure used to estimate the statistical distribution of angles, each one defined by a couple of unit vectors. In particular, we want to point out that when presenting angle statistic, we count the number of cosine occurrences and detail the way in which averages, variances, and other statistical parameters are calculated.

There are two reasons for performing statistics on angle cosines. First, orienting $\mathbf{e}_z$ along one of the unit vectors, any other unit vector would point somewhere on the surface of the sphere of unitary radius centered at the origin. Defining the colatitude angle θ as for usual spherical reference frames, the angle interval between θ and θ+dθ individuates an area of 2π sin(θ) dθ on the surface of the sphere. Hence, values of the angle θ between uncorrelated unit vectors are distributed proportionally to sin(θ), so that values of cos(θ) are uniformly distributed whenever one of the two unit vectors moves randomly with respect to the other. Therefore, any peak in the occurrence distribution of cos(θ) can be considered the signature of some correlation between non-random unit vectors. Secondly, it is immediate to deal with unit vectors defined least for sign (such as MCA eigenvectors) when considering cos(θ) distributions. Indeed, if one of the unitary vectors is defined least for its orientation, then values of θ and π-θ must be considered as equivalent: it is immediate to do this when considering cosine distributions, since|cos(θ)|=|cos(π-θ)|.

Statistical parameters such as averages, variances, and medians of the θ distribution are obtained by applying the arccos function to the corresponding quantities calculated from the cosine distributions.

Appendix C: Comparison Between MDD, MRA, and MCA Performances on the Same Event

Here we shortly discuss how MDD, MRA, and MCA do perform on the same event. For this experiment (or exercise) we choose the event studied in Lavraud et al. (2016), an event that displays a great variation in magnetic field magnitude and therefore can highlight at best the differences among MDD, MRA, and MCA outcomes. In Figure A1, panels (a) to (d) show characteristic plasma quantities: magnetic field, current density, ion velocity, and pressures. Panels (e) to (h) show MDD, MRA, and MCA eigenvalues, respectively, along with the shape factors elongation and planarity defined as in section 1 relative to MCA but valid also for MDD (note that if we had to calculate the MRA shape factors, only planarity would have sense since elongation would always stick to one). The accuracy threshold follows the definition given in section 3 for the cases of MRA and MCA, while for MDD we take out the squared field intensity at the denominator. Now, by examining MCA results as from section 4 in the main text, one can easily recognize the presence of some small-scale configuration traversed between 10:33:27 and 10:33:28, whose shape somewhat oscillates between knife-blade and pancake since planarity is in general close to one and elongation behaves unsteadily. The notable similarity between MRA and MCA results points out that the greatest contribution to the magnetic field gradient is given by differences in the direction of **B** between one spacecraft and the others, while differences in magnitude are in general less important. Average magnitude, however, is of fundamental importance since by neglecting its effects (that is, when performing MDD) one ends up losing track of some relevant features in magnetic configurations (like the small-scale region pointed out before).

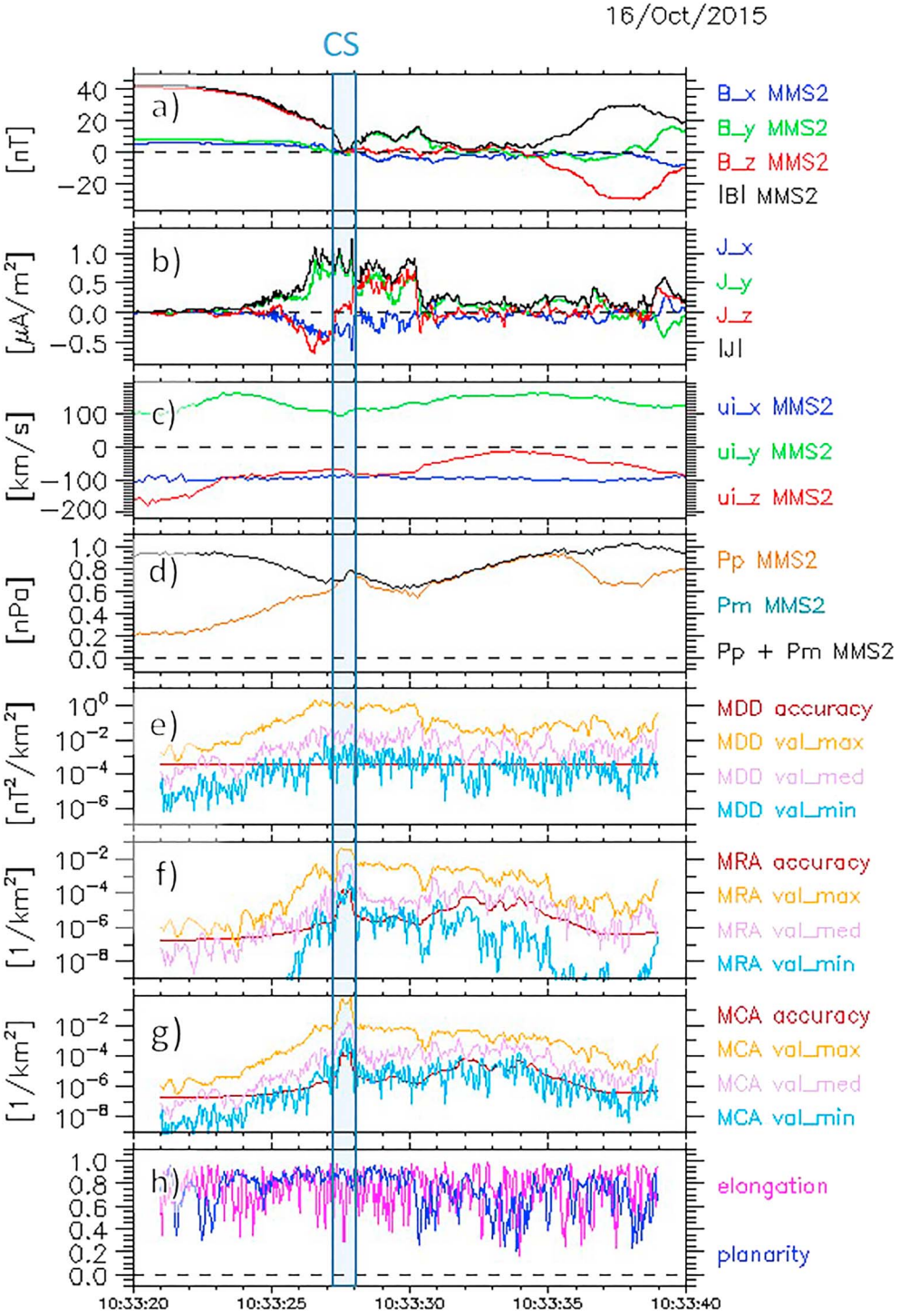

Figure A1. Data recorded by MMS2 between 11:33:20 and 11:33:40 UT on 16 October 2015, and results of the (four spacecraft) magnetic directional derivative (MDD), magnetic rotational analysis (MRA), and magnetic configuration analysis (MCA) analyses on the same data interval. This event was studied in Lavraud et al. (2016). The four upper panels show characteristic plasma quantities: (a) magnetic field, (b) current from particle measurements, (c) bulk ion flow (in geocentric solar equatorial coordinates), and (d) the three plasma "pressures" (thermal, magnetic and total). The four lower panels display MCA results: (e) MDD eigenvalues, (f) MRA eigenvalues, (g) MCA eigenvalues, and (h) shape parameters ($\mathscr{E}$ and $\mathscr{P}$) referred to MCA (or, equivalently, to MDD). Note that the additional line in the eigenvalue plot estimates the expected accuracy threshold (see section 3 for its definition in the MRA and MCA cases—for MDD its definition is the same as in the other situations, least for the square of field intensity at the denominator). Notice that MCA shows the presence of very small scales between 11:33:27 and 11:33:28, while MRA only partially recognizes this and MDD does not consider it at all. The overall planar character of magnetic configurations traversed between 11:33:25 and 11:23:32 is also evident.

Acknowledgments

Work at IRAP was supported by CNRS and CNES. We wish to acknowledge support from the International Space Science Institute, Bern. This work was partially supported by MMS contract 499878Q. We thank Emmanuel Penou at IRAP for developing the CL tool (http://clweb.irap.omp.eu/), which was used to plot the MMS data in Figures 2, 3, and A1 in the main paper, and all figures from S3 to S7 in the supporting information. MMS data are available at https://lasp.colorado.edu/mms/sdc/public/and at http://clweb.irap.omp.eu/.

References

Angelopoulos, V. (2008). The THEMIS mission. *Space Science Reviews*, *141*(1-4), 5–34. https://doi.org/10.1007/s11214-008-9336-1

Baker, D. N., Riesberg, L., Pankratz, C. K., Panneton, R. S., Giles, B. S., Wilder, F. D., & Ergun, R. E. (2016). Magnetospheric Multiscale instrument suite operations and data system. *Space Science Reviews*, *199*(1-4), 545–575. https://doi.org/10.1007/s11214-014-0128-5

Burch, J. L., Moore, T. E., Torbert, R. B., & Giles, B. L. (2016). Magnetospheric Multiscale overview and science objectives. *Space Science Reviews*, *199*(1-4), 5–21. https://doi.org/10.1007/s11214-015-0164-9

Chanteur, G. (1998). Spatial interpolation for four spacecraft: Theory. In G. Paschmann & P. W. Daly (Eds.), *Analysis methods for multi-spacecraft data* (Vol. 7, pp. 929–939). Noordwijk, Netherlands: ESA Publications. https://doi.org/10.1517/13543784.7.6.929

Chasapis, A., Yang, Y., Matthaeus, W. H., Parashar, T. N., Haggerty, C. C., Burch, J. L., et al. (2018). Energy Conversion and Collisionless Plasma Dissipation Channels in the Turbulent Magnetosheath Observed by the Magnetospheric Multiscale Mission. *The Astrophysical Journal*, *862*, 32. https://doi.org.10.3847/1538-4357/aac775

Denton, R. E., Sonnerup, B. U. Ö., Birn, J., Teh, W.-L., Drake, J. F., Swisdak, M., & Hesse, M. (2012). Test of Shi et al. method to infer the magnetic reconnection geometry from spacecraft data: MHD simulation with guide field and antiparallel kinetic simulation. *Journal of Geophysical Research*, *117*, A09201. https://doi.org/10.1029/2012JA017877

Denton, R. E., Sonnerup, B. U. Ö., Birn, J., Teh, W.-L., Drake, J. F., Swisdak, M., et al. (2010). Test of methods to infer the magnetic reconnection geometry from spaccraft data. *Journal of Geophysical Research*, *115*, A10242. https://doi.org/10.1029/2010JA015420

Denton, R. E., Sonnerup, B. U. Ö., Hasegawa, H., Phan, T. D., Russell, C. T., Strangeway, R. J., et al. (2016). Motion of the MMS spacecraft relative to the magnetic reconnection structure observed on 16 October 2015 at 1307 UT. *Geophysical Research Letters*, *43*, 5589–5596. https://doi.org/10.1002/2016GL069214

Denton, R. E., Sonnerup, B. U. Ö., Russell, C. T., Hasegawa, H., Phan, T. D., Strangeway, R. J., et al. (2018). Determining L-M-N current sheet coordinates at the magnetopause from Magnetospheric Multiscale data. *Journal of Geophysical Research: Space Physics*, *123*, 2274–2295. https://doi.org/10.1002/2017JA024619

Eastwood, J. P., Phan, T. D., Cassak, P. A., Gershman, D. J., Haggerty, C., Malakit, K., et al. (2016). Ion-scale secondary flux ropes generated by magnetopause reconnection as resolved by MMS. *Geophysical Research Letters*, *43*, 4716–4724. https://doi.org/10.1002/2016GL068747

Escoubet, C., Schmidt, R., & Goldstein, M. (1997). Cluster—Science and mission overview. *Space Science Reviews*, *79*. https://doi.org/10.1023/A:1004923124586

Kacem, I., Jacquey, C., Génot, V., Lavraud, B., Vernisse, Y., Marchaudon, A., et al. (2018). Magnetic reconnection at a thin current sheet separating two interlaced flux tubes at the Earth's magnetopause. *Journal of Geophysical Research: Space Physics*, *123*, 1779–1793. https://doi.org/10.1002/2017JA024537

Lavraud, B., Zhang, Y. C., Vernisse, Y., Gershman, D. J., Dorelli, J., Cassak, P. A., et al. (2016). Currents and associated electron scattering and bouncing near the diffusion region at Earth's magnetopause. *Geophysical Research Letters*, *43*, 6036–6043. https://doi.org/10.1002/2016GL068359

Parker, E. N. (2004). Tangential discontinuities in untidy magnetic topologies. *Physics of Plasmas*, *11*(5), 2328–2332. https://doi.org/10.1063/1.1646674

Pollock, C., Moore, T., Jacques, A., Burch, J., Gliese, U., Saito, Y., et al. (2016). Fast plasma investigation for Magnetospheric Multiscale. *Space Science Reviews*, *199*(1-4), 331–406. https://doi.org/10.1007/s11214-016-0245-4

Rappazzo, A. F. (2015). Equilibria, dynamics and current sheet formation in magnetically confined coronae. *The Astrophysical Journal*, *815*(1). https://doi.org/10.1088/0004-637X/815/1/8

Rappazzo, A. F., & Parker, E. N. (2013). Current sheet formation in tangled coronal magnetic fields. *The Astrophysical Journal Letters*, *773*(1), L2. https://doi.org/10.1088/2041-8205/773/1/L2

Rezeau, L., Belmont, G., Manuzzo, R., Aunai, N., & Dargent, J. (2018). Analyzing the magnetopause internal structure: New possibilities offered by MMS tested in a case study. *Journal of Geophysical Reseach: Space Physics*, *123*, 227–241. https://doi.org/10.1002/2017JA024526

Robert, P., Roux, A., Harvey, C. C., Dunlop, M. W., Daly, P. W., & Glassmeier, K.-H. (1998). Tetrahedron Geometric Factors). In G. Paschmann & P. W. Daly (Eds.), *Analysis methods for multi-spacecraft data* (Vol. 7, pp. 929–939). Noordwijk, Netherlands: ESA Publications. https://doi.org/10.1517/13543784.7.6.929

Russell, C. T., Anderson, B. J., Baumjohann, W., Bromund, K. R., Dearborn, D., Fischer, D., et al. (2016). The Magnetospheric Multiscale magnetometers. *Space Science Reviews*, *199*(1-4), 189–256. https://doi.org/10.1007/s11214-014-0057-3

Shen, C., Li, X., Dunlop, M., Shi, Q. Q., Liu, Z. X., Lucek, E., & Chen, Z. Q. (2007). Magnetic field rotation analysis and the applications. *Journal of Geophysical Research*, *112*, A06211. https://doi.org/10.1029/2005JA011584

Shen, C., Li, X., Dunlop, M. W., Liu, Z. X., Balogh, A., Baker, D. N., et al. (2003). Analyses on the geometrical structure of magnetic field in the current sheet based on cluster measurements. *Journal of Geophysical Research*, *108*(A5), 1168. https://doi.org/10.1029/2002JA009612

Shi, Q. Q., Shen, C., Dunlop, M. W., Pu, Z. Y., Zong, Q.-G., Liu, Z.-X., et al. (2006). Motion of observed structures calculated from multi-point magnetic field measurements: Application to Cluster. *Geophysical Research Letters*, *33*, L08109. https://doi.org/10.1029/2005GL025073

Shi, Q. Q., Shen, C., Pu, Z. Y., Dunlop, M. W., Zong, Q.-G., Zhang, H., et al. (2005). Dimensional analysis of observed structures using multipoint magnetic field measurements: Application to Cluster. *Geophysical Research Letters*, *32*, L12105. https://doi.org/10.1029/2005GL022454

Taylor, J. B. (2000). Relaxation revisited. *Physics of Plasmas*, *7*(5), 1623–1629. https://doi.org/10.1063/1.873984

Tooley, C. R., Black, R. K., Robertson, B. P., Stone, J. M., Pope, S. E., & Davis, G. T. (2015). The Magnetospheric Multiscale constellation. *Space Science Reviews*, *199*(1-4), 23–76. https://doi.org/10.1007/s11214-015-0220-5

Zhang, L., He, J., Tu, C., Yang, L., Wang, X., Marsch, E., & Wangg, L. (2015). Occurrence rates and heating effects of tangential and rotational discontinuities as obtained from three-dimensional simulation of magnetohydrodynamic turbulence. *The Astrophysical Journal Letters*, *804*(2), L43. https://doi.org/10.1088/2041-8205/804/2/L43

Zhou, M., Berchem, J., Walker, R. J., El-Alaoui, M., Goldstein, M. L., Lapenta, G., et al. (2018). Magnetospheric Multiscale observations of an ion diffusion region with large guide field at the magnetopause: Current system, electron heating, and plasma waves. *Journal of Geophysical Research: Space Physics*, *123*, 1834–1852. https://doi.org/10.1002/2017JA024517

References From the Supporting Information

Chasapis, A., Matthaeus, W. H., Parashar, T. N., LeContel, O., Retinò, A., & Breuillard, H. (2017). Electron heating at kinetic scales in magnetosheath turbulence. *The Astrophysical Journal*, *836*(2), 247. https://doi.org/10.3847/1538-4357/836/2/247

Fuselier, S. A., Vines, S. K., Burch, J. L., Petrinec, S. M., Trattner, K. J., Cassak, P. A., et al. (2017). Large-scale characteristics of reconnection diffusion regions and associated magnetopause crossings observed by MMS. *Journal of Geophysical Research: Space Physics*, *122*, 5466–5486. https://doi.org/10.1002/2017JA024024

Huang, S. Y., Du, J. W., Sahraoui, F., Yuan, Z. G., He, J. S., Zhao, J. S., et al. (2017). A statistical study of kinetic-size magnetic holes in turbulent magnetosheath: MMS observations. *Journal of Geophysical Research: Space Physics*, *122*, 8577–8588. https://doi.org/10.1002/2017JA024415

Huang, S. Y., Sahraoui, F., Yuan, Z. G., He, J. S., Zhao, J. S., Le Contel, O., et al. (2017). Magnetospheric Multiscale observations of electron vortex magnetic hole in the turbulent magnetosheath plasma. *The Astrophysical Journal Letters*, *836*(2), L27. https://doi.org/10.3847/2041-8213/aa5f50

Hwang, K.-J., Sibeck, D. G., Burch, J. L., Choi, E., Fear, R. C., Lavraud, B., et al. (2018). Small-scale flux transfer events formed in the reconnection exhaust region between two X lines. *Journal of Geophysical Research: Space Physics*, *123*, 8473–8488. https://doi.org/10.1029/2018JA025611

Øieroset, M., Phan, T. D., Haggerty, C., Shay, M. A., Eastwood, J. P., Gershman, D. J., et al. (2016). MMS observations of large guide field symmetric reconnection between colliding reconnection jets at the center of a magnetic flux rope at the magnetopause. *Geophysical Research Letters*, *43*, 5536–5544. https://doi.org/10.1002/2016GL069166

Vogt, J., & Paschmann, G. (1998). Accuracy of Plasma Moment Derivatives. In G. Paschmann & P. W. Daly (Eds.), *Analysis methods for multi-spacecraft data* (Vol. 7, pp. 929–939). Noordwijk, Netherlands: ESA Publications. https://doi.org/10.1517/13543784.7.6.929

Webster, J. M., Burch, J. L., Reiff, P. H., Daou, A. G., Genestreti, K. J., Graham, D. B., et al. (2018). Magnetospheric Multiscale dayside reconnection electron diffusion region events. *Journal of Geophysical Research: Space Physics*, *123*, 4858–4878. https://doi.org/10.1029/2018JA025245